ACS SENSORS

pubs.acs.org/acssensors

Article

Nanoporous Gold for the Miniaturization of In Vivo Electrochemical Aptamer-Based Sensors

Alex M. Downs, Julian Gerson, M. Nur Hossain, Kyle Ploense, Michael Pham, Heinz-Bernhard Kraatz, Tod Kippin, and Kevin W. Plaxco*

Cite This: *ACS Sens.* 2021, 6, 2299−2306

Read Online

ACCESS | Metrics & More | Article Recommendations | Supporting Information

ABSTRACT: Electrochemical aptamer-based sensors enable real-time molecular measurements in the living body. The spatial resolution of these measurements and ability to perform measurements in targeted locations, however, is limited by the length and width of the device's working electrode. Historically, achieving good signal to noise in the complex, noisy in vivo environment has required working electrode lengths of 3−6 mm. To enable sensor miniaturization, here we have enhanced the signaling current obtained for a sensor of given macroscopic dimensions by increasing its surface area. Specifically, we produced nanoporous gold via an electrochemical alloying/dealloying technique to increase the microscopic surface area of our working electrodes by up to 100-fold. Using this approach, we have miniaturized in vivo electrochemical aptamer-based (EAB) sensors (here using sensors against the antibiotic, vancomycin) by a factor of 6 while retaining sensor signal and response times. Conveniently, the fabrication of nanoporous gold is simple, parallelizable, and compatible with both two- and three-dimensional electrode architectures, suggesting that it may be of value to a range of electrochemical biosensor applications.

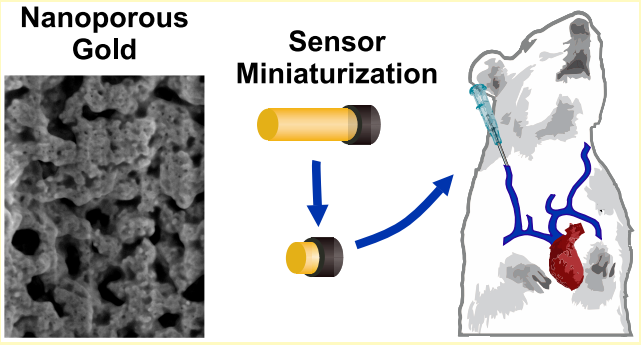

KEYWORDS: *nanoporous gold, aptamer, biosensor, miniaturization, electrochemical, square wave voltammetry, in vivo, sensor*

Electrochemical aptamer-based (EAB) sensors are the first technology able to perform in vivo molecular measurements irrespective of the chemical (e.g., enzymatic, redox, spectroscopic) properties of the target analyte.[1] To date, these sensors have enabled detection of a range of targets, such as pharmaceuticals,[1−3] drugs of abuse,[4] proteins,[5−7] and amino acids.[8,9] EAB sensors consist of an electrode-attached, redox reporter-labeled aptamer that binds to its target species. Upon target binding, a conformational change drives a change in electron-transfer kinetics between the redox reporter and electrode surface[10] (Figure 1A). This reversible signal transduction mechanism renders EAB sensors both continuous and selective enough to deploy in the living body.[1,5,11] Previously, EAB sensors have proven useful for real-time monitoring a range of drugs and metabolites in living rats; their real-time target quantification has even enabled performance of closed-loop, feedback-controlled drug delivery.[2,12]

Achieving good signal to noise in the complex environments found in vivo has historically required 75−200 μm diameter gold wires with lengths of 3−6 mm (refs1, 2, 5, 12−14). And while such sensors are small relative to the length scale of human tissue dimensions, they are inconveniently large for some applications. The lengths of the sensors in prior use limit our ability to make targeted measurements in specific rat brain regions. Likewise, intravenous deployment of EAB sensors in mice, an animal model of great interest for pharmaceutical screening, would require narrower sensors. Thus motivated, we explore here a new approach to further miniaturizing in vivo EAB sensors.

Because it allows the attachment of more aptamers to an electrode of a given size, increasing the microscopic surface area of the gold provides a route toward smaller EAB sensors. To this end, many techniques exist that enhance the microscopic surface area of gold, including a number of electrochemical etching/deposition approaches,[15−22] co-sputtering,[23−25] or the leaching of commercially available gold alloy foils.[23,26,27] Co-sputtering and the leaching of gold foil, however, are incompatible with the wire format of our implantable sensors. In contrast, electrochemical surface area enhancement techniques are readily compatible with our sensor architecture. Indeed, our prior in vivo EAB studies

Received: February 18, 2021
Accepted: May 6, 2021
Published: May 26, 2021

https://doi.org/10.1021/acssensors.1c00354
ACS Sens. 2021, 6, 2299−2306

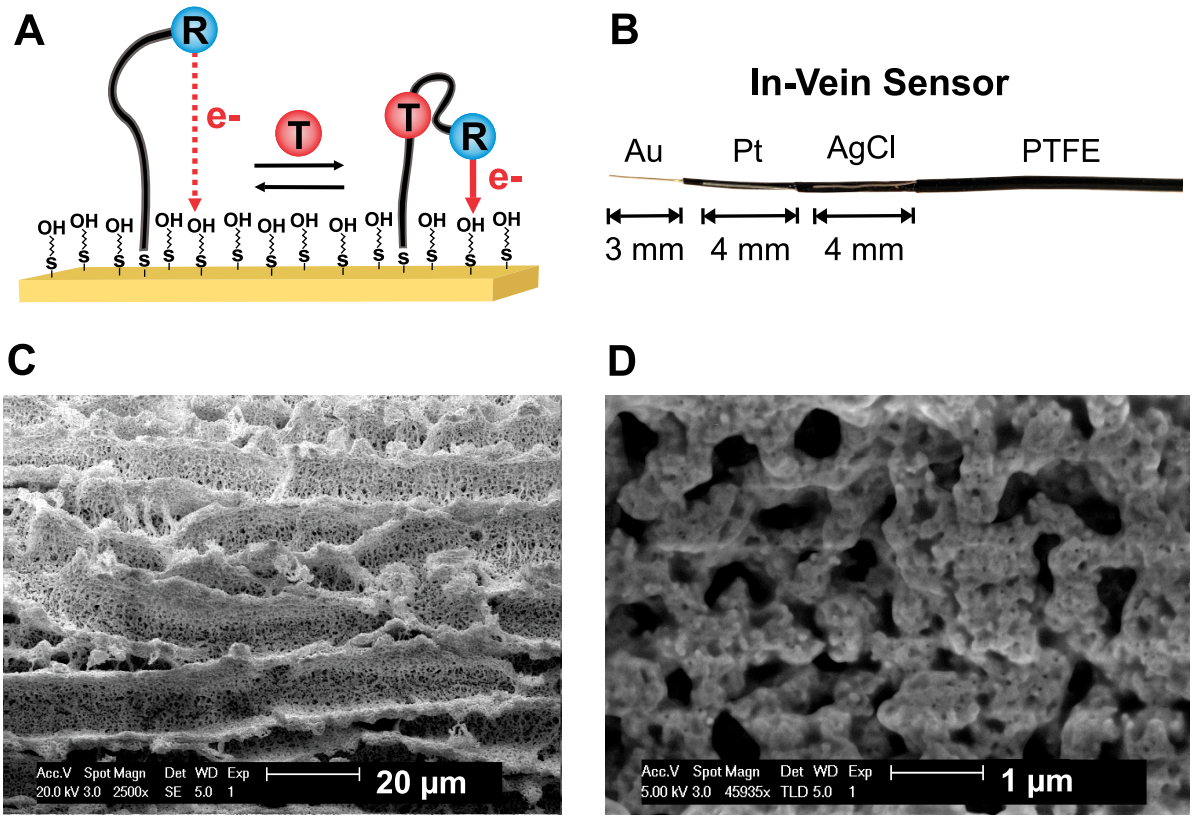

Figure 1. (A) To fabricate an EAB sensor, we form a self-assembled monolayer consisting of redox reporter-modified (R) aptamers and 6-mercapto-1-hexanol on the surface of a gold electrode. EAB signaling occurs via a target (T) binding-induced change in the electron-transfer kinetics of the redox reporter. Graphic reprinted with permission.[28] (B) Our intravenous EAB sensors consist of bundled gold, platinum, and silver wires. In the past work, in vivo measurements have required gold working electrodes measuring 3−6 mm in length and 75−200 μm in diameter. (C) To further miniaturize EAB sensors, here we have fabricated them using nanoporous gold electrodes. As shown by scanning electron microscopy at 2500× magnification, layers of sponge-like pores cover the surface of these electrodes, greatly increasing their microscopic surface area. (D) As shown by scanning electron microscopy at 45935× magnification, the matrix pore sizes range from 30 to 500 nm.

relied on electrochemical roughening in acid to produce dendritic structures. However, this technique achieves only 2- to 4-fold enhancements.[14] Here, in contrast, we have implemented an electrochemical alloying and dealloying process that achieves up to a 100-fold increase in surface area, enabling significant reductions in the EAB sensor size.

MATERIALS AND METHODS

Electrode Fabrication. For in vitro experiments, we fabricated sensors by soldering a 5 cm long gold wire (For Figures 2 and 3: 200 μm diameter from Alfa Aesar, Haverhill, MA. For Figures 4 and 5: 75 μm diameter from A-M Systems, Sequim, WA) to a gold-plated pin connector (CH Instruments, Inc., Austin, TX) with a 60/40 lead−selenium solder (Digikey, Thief River Falls, MN). We isolated the desired length at the end of the gold wire by insulating with a layer of poly(tetrafluoroethylene) (PTFE) heat-shrink tubing (HS Sub-Lite-Wall PTFE, ZEUS, Orangeburg, SC) with an industrial hot air blower (Master Appliance Corp., Racine, WI).

For in vivo experiments, we fabricated the sensor probe by bundling 7.5 cm long, 75 μm diameter gold, platinum, and silver wires (A-M Systems, Sequim, WA) together using the same PTFE heat-shrink tubing used for in vitro sensors. Using a digital caliper and a razor blade, we trimmed the lengths of the exposed wire to measure 0.5, 4, and 4 mm for the gold, platinum, and silver wires, respectively. To prevent contact between the wires, we left a ∼0.75 mm gap between each. To form a reference electrode, we deposited an AgCl layer on the silver wire by immersing the wire bundle in a concentrated sodium hypochlorite solution (Chlorox bleach) for at least 1 h. We rinsed the bundled wires in deionized water, electrochemically cleaned them, and modified them with the aptamer and surface assembled monolayer, as described below. Care was taken to avoid immersing the reference electrode into the NaOH or H_2SO_4 solutions used in subsequent steps, as these can damage the AgCl layer.

Electrode Electrochemical Cleaning. For electrode cleaning and in vitro characterization, our electrochemical cell consisted of a PTFE-wrapped gold sensor working electrode, a platinum counter electrode (CH Instruments, Inc, Austin, TX), and a AglAgCl reference electrode (CH Instruments, Inc., Austin TX). We secured our working, counter, and reference electrodes in a cell vessel "shot glass" with a custom-fabricated Teflon lid fixture (see Figure 3A). First, we electrochemically cleaned the electrodes in 0.5 M NaOH (Sigma-Aldrich, St. Louis, MO) by performing repeated cyclic voltammetry scans between −1 and −1.6 V (all potentials versus AglAgCl) at the 1 V s^{-1} scan rate for 300 cycles using a CH Multipotentiostat (CHI1040C, CH Instruments, Inc.). We rinsed the electrodes in deionized water and then immersed them in 50 mM H_2SO_4 (Sigma-Aldrich, St. Louis, MO). We recorded a series of five cyclic voltammograms in 50 mM H_2SO_4 (sweeping between 0 and 1.8 V at 0.1 V s^{-1}). To determine the electrode surface area, we measured the area under the cyclic voltammogram curve associated with the gold oxide reduction peak and divided it by the charge density of a monolayer of chemisorbed oxygen on gold (∼400 μC cm^{-2}, see ref 14). We then rinsed the electrodes in deionized water.

Nanoporous Gold Deposition and Surface Area Measurements. We dissolved 1.5 M $ZnCl_2$ (≥98%, Sigma-Aldrich, St. Louis, MO) in anhydrous ethylene glycol (99.8%, Sigma-Aldrich, St. Louis, MO) by alternatively heating (at 115 °C in a mineral oil bath) and vortexing the mixture. The solution was then added to the

https://doi.org/10.1021/acssensors.1c00354
ACS Sens. 2021, 6, 2299−2306

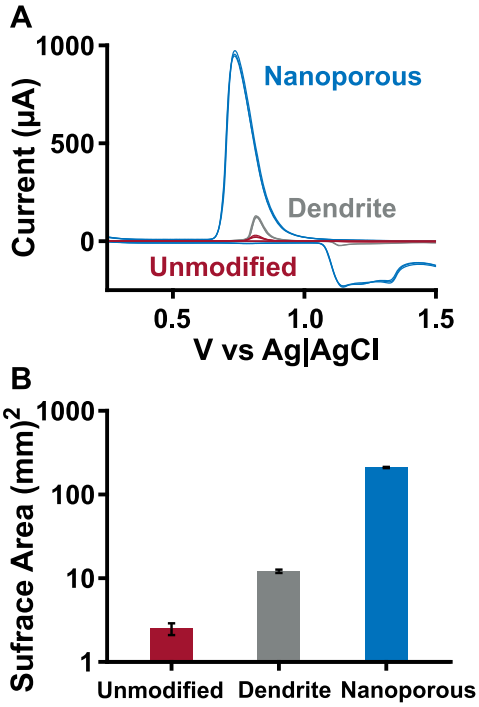

Figure 2. Generation of nanoporous gold greatly increases the microscopic surface area of gold wire electrodes. To see this, we used cyclic voltammetry (CV) to compare the microscopic surface areas of three wire substrates: unmodified gold wire, dendrite-covered wire prepared using our prior electrochemical roughening procedure,[14] and nanoporous gold wire of the type explored here. Each wire has an exposed working electrode surface 3 mm long by 200 μm in diameter. (A) Comparing the areas under CV curves collected in 50 mM sulfuric acid (which reflects the reduction of the gold oxide surface layer,[32] which, in turn, is proportional to the microscopic surface area[14,33]) of the three surface morphologies, we see that the microscopic surface areas of the nanoporous substrate are greatly enhanced. Of note, this figure shows data collected from three electrodes for each morphology; the curves overlap well, illustrating the reproducibility of our fabrication procedures. (B) Integrated areas under the reduction peak in the CV curves shown in the prior panel indicate that the surface area of this batch of nanoporous gold electrodes is approximately 85-fold greater than that of the unmodified gold and 20-fold greater than that of the dendritic gold. The error bars here and elsewhere in this manuscript reflect standard deviations of the mean.

electrochemical cell, covered with a 0.5 cm layer of mineral oil, and immersed in a mineral oil bath heated to 115 °C. As both counter and reference electrodes, we inserted ~0.75 cm wide pieces of a zinc foil (0.25 mm thick, 99.9% trace metals basis, Sigma-Aldrich, St. Louis, MO), which had been sanded with a file, rinsed thoroughly in deionized water, and dried prior to use. We then connected the reference electrode, the counter electrode, and up to six gold wire working electrodes in series to a CHI1040C multipotentiostat (CH Instruments, Inc., Austin TX). To perform alloying, we scanned the working electrodes with a cyclic voltammogram starting at 0 V and then scanning from 0.8 to 1.8 V at 0.01 V s^{-1}. We repeated this 10 times (Figure S1) before removing the working electrodes and rinsing them with deionized water. To remove the zinc from the alloy, we next immersed the working electrodes in 5 M HCl (Merck, Darmstadt, Germany) for 15 min with magnetic stir bar agitation. The electrodes were then removed and rinsed in deionized water.

To complete the dealloying process, we placed the electrodes in 50 mM H_2SO_4 and applied cyclic voltammetry (scanning between 0 and 1.8 V at 0.1 V s^{-1}) until residual Zn is removed and the reduction peaks appear consistent in height and area. Typically, this takes 5 to 15 cyclic voltammetry scans (see Figure S2). Using the area of the gold oxide reduction peak, we again calculate the electrode surface area. Dividing this by the original unmodified area provides the area enhancement factor.

To assess surface morphology and pore size, we captured images of the nanoporous gold using a FEI XL-30 Sirion scanning electron microscope. To do so, we trimmed a portion of gold, affixed it to a mount with a copper adhesive tape, and imaged at a 2500× magnification and then a 45 935× magnification. We used ImageJ's set scale and linear measure feature to estimate the pore size using the scanning electron microscopy (SEM) detail image in Figure 1D.

EAB Sensor Fabrication. We first thawed a 2 μL aliquot of the 100 μM aptamer (sequence below) modified with a 6-carbon thiol linker on the 5′ end and a methylene blue on the 3′ end (Biosearch Technologies, Novato, CA, dual HPLC purification, stored at −20 °C).

Vancomycin Aptamer. 5′−SH−$(CH_2)_6$−CGAGG GTACC GCAAT AGTAC TTATT GTTCG CCTAT TGTGG GTCGG−O−CH_2−$CHCH_2OH$−$(CH_2)_4$−NH−CO−$(CH_2)_2$−methylene blue-3′

Because the manufacturer provides the DNA constructs in oxidized form, which do not effectively immobilize onto the gold surface, we must reduce the disulfide bond before deposition. To do so, we combined 2 μL of 10 mM Tris (2-carboxyethyl) phosphine (TCEP, Sigma-Aldrich, St. Louis, MO) with the aptamer sample for a 1 h thiol reduction in the dark at room temperature. We then diluted the sample with 96 μL of 1× phosphate-buffered saline (PBS, ChemCruz 20X phosphate-buffered saline, Santa Cruz Biotechnology, Dallas, TX) and quantified the concentration of the aptamer using the molar absorption coefficient at 260 nm (provided by the supplier) with UV−vis spectroscopy (DU800, Beckman Coulter, Brea, CA). Using PBS, we then diluted the aptamer to 1 μM.

As the final step in sensor fabrication, we placed the freshly cleaned gold electrodes in the prepared aptamer solution for 1 h at room temperature in the dark. To passivate the surface, we then rinsed the electrodes with deionized water and immersed them for 12−18 h at room temperature in a freshly-prepared 10 mM 6-mercapto-1-hexanol solution (Sigma-Aldrich, St. Louis, MO) in 1× PBS. Following a final rinse with deionized water, the sensors were ready for use.

In Vitro Experiments. We filled the electrochemical cell with PBS, rinsed the electrodes in deionized water, and secured them in the electrochemical cell's Teflon cap. We collected a baseline cyclic voltammogram in PBS (−0.1 to −0.5 V, 0.1 V s^{-1}). We calculate the redox reporter charge transfer in coulombs using the area determination feature of the CH potentiostat software, which quantifies charge transfer using the area of the reduction peak and the cyclic voltammogram scan rate. We moved the electrode cap to the selected media (PBS or heparinized bovine blood, acquired from Hemostat Laboratories, Dixon, CA) and performed repeated square wave voltammetry scans (−0.2 to −0.4 V, 25 mV amplitude) at a frequency where the square wave voltammetry peak signal decreases in response to the target ("signal-off," here 10 Hz) and a frequency where the square wave voltammetry peak signal increases in response the to target ("signal-on," here 60 Hz). It is common to observe a downward drift in square wave voltammogram peak current, especially in complex media, such as whole blood. To correct for any peak signal loss, we applied a previously described drift correction technique termed "Kinetic Differential Measurements (KDM)".[1,12,29] In KDM, the normalized signal-off peak currents are subtracted from the signal-on peak currents. When these two signals drift roughly in concert, this enables correction of drift in complex environments.

In Vivo Experiments. For in vivo experiments, we prepared our sensors by inserting the wire bundle probes into a 22 gauge catheter (BD Insyte Autoguard shielded IV catheter, BD, Franklin Lakes, NJ) that has ~2 mm windows cut into the catheter wall to expose the platinum and AgCl wires. To prevent air bubbles in the catheter, a syringe with a 27 gauge needle was used to fill the syringe with PBS. Once filled, we inserted the syringe into a PBS-containing electrochemical cell and collected a cyclic voltammogram (−0.1 to

https://doi.org/10.1021/acssensors.1c00354
ACS Sens. 2021, 6, 2299−2306

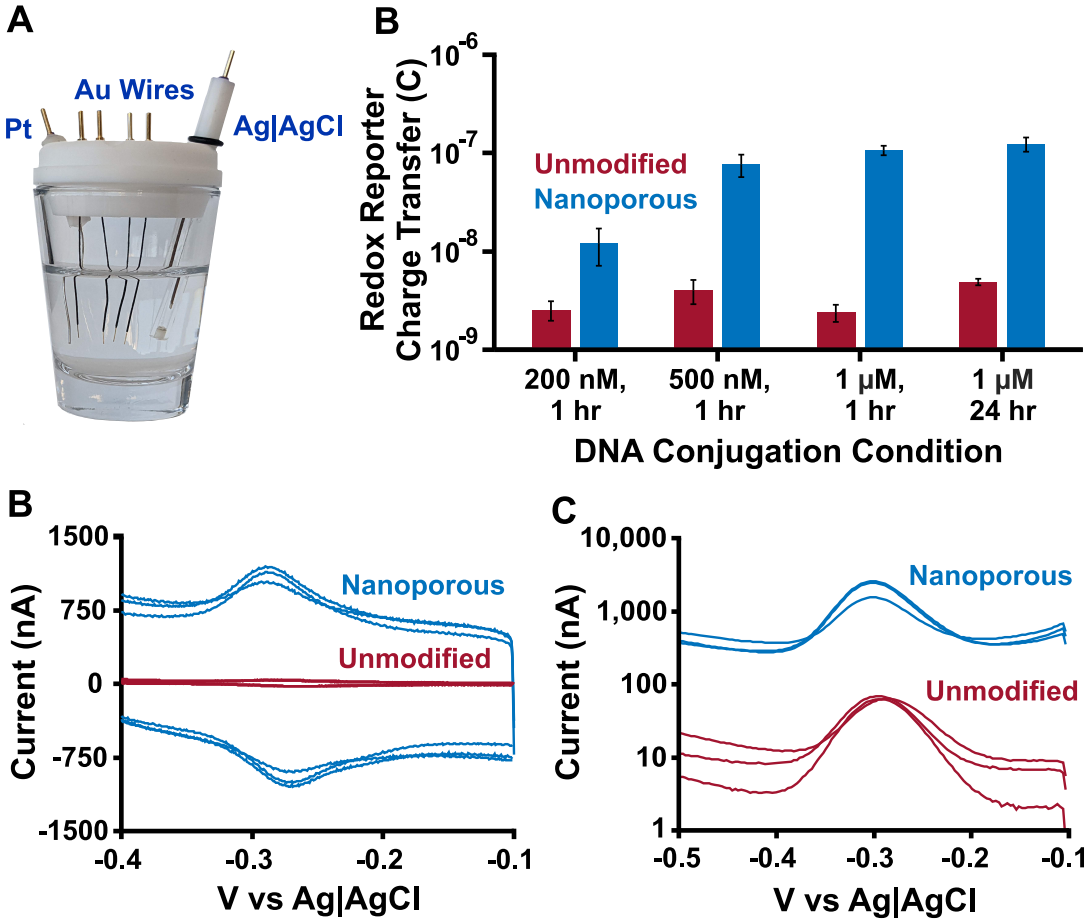

Figure 3. Irrespective of the aptamer deposition conditions, nanoporous substrates produce higher EAB sensor signals than unmodified substrates of the same macroscopic dimensions. (A) We interrogate EAB sensors in PBS within a glass vessel, using a PTFE cap to secure the gold wire working electrodes, platinum counter electrode, and Ag|AgCl reference electrode. (B) Charge transfer from the redox reporter (a measure of the number of methylene blue-modified aptamers on the surface) is higher for the nanoporous electrodes at all aptamer deposition concentrations and durations. Here, we incubated independently prepared electrodes with the thiol-modified aptamer at 200 nM, 500 nM, or 1 μM for 1 h and at 1 μM for 24 h (n = 3 electrodes each). Because the increase in charge transfer plateaus at a 1 h long, 1 μM DNA deposition, we select these as our deposition conditions. (C) Increase in the redox signal produced by nanoporous electrodes is evident here in the cyclic voltammograms. For the same macroscopic dimensions (3 mm long × 200 μm diameter, n = 3 each), the methylene blue redox peak area is 25-fold greater for nanoporous electrodes. (D) Reflecting this, the square wave voltammetry peaks of sensors fabricated on nanoporous electrodes also increase significantly. At a square wave frequency of 10 Hz, for example, the nanoporous wires exhibit approximately 30-fold greater peak currents (note that the y-axis on this plot is logarithmic).

−0.5 V versus AgCl wire, or Ag|AgCl frit reference) to confirm the presence of the aptamer signal and a well-formed monolayer.

The Institutional Animal Care and Use Committee (IACUC) of the University of California at Santa Barbara approved our experimental protocol, which adhered to the guidelines provided by the NIH Guide for Care and Use of Laboratory Animals (8th edition, National Academy Press, 2011).[30] The Sprague Dawley rats weighed 660−760 g and were pair-housed in a 12:12 standard light cycle room with ad libitum access to food and water.

We surgically inserted the sensor-catheter assembly into the right jugular vein of a Sprague Dawley rat (Charles River Laboratories, Santa Cruz, CA), as described previously.[1,11,12] Briefly, we shaved the chest area above the right and left jugular veins and cleaned the skin using betaine and 70% ethanol. We anesthetized the rat using 5% isoflurane in a plexiglass anesthesia chamber and then maintained 2−3% isoflurane/oxygen anesthesia throughout the experiment using a nose cone.

To enable delivery of vancomycin (100 mM in filtered PBS), we installed a silastic catheter and infusion line into the left jugular vein as previously described[1] using a steel cannula with a screw-type connector (Plastics One, Roanoke, VA) and silastic tubing (11 cm, i.d. 0.64 mm, o.d. 1.19 mm, Dow Corning, Midland, MI). We secured the sensor and infusion lines using a sterile 6-0 silk suture (Fine Science Tools, Foster City, CA) and manually infused 30 units of heparin into the venous system prior to electrochemical measurements. We then connected the infusion line to a syringe of 100 mM vancomycin positioned on a syringe pump (KDS 200, KD Scientific Inc., Holliston, MA).

Using alligator clips, we connected the sensor probe to the potentiostat (for single-sensor experiments, we used the single-channel CHI1242B; for multiplexed experiments, such as Figure S3, we used the multichannel CHI1040C). To confirm sensor connection and proper function, we first collected a cyclic voltammogram and baseline square wave voltammogram at 10 Hz. We continuously recorded square wave voltammograms at signal-off (10 Hz for both nanoporous and dendrite) and signal-on (60 Hz for nanoporous, 300 Hz for dendrite) frequencies, using a previously described python script[31] to plot data in real time. After collecting a 15−30 min baseline, we used the syringe pump to inject a 40 mg kg^{-1} dose of vancomycin at a rate of 0.1 mL min^{-1}.

Data Analysis. To analyze square wave voltammetry peak currents in real time, we used a previously reported, open source python script.[31] When provided with voltammogram bounds (typically, −0.21 to −0.39 V) and desired Savitzky−Golay filtering

https://doi.org/10.1021/acssensors.1c00354
ACS Sens. 2021, 6, 2299−2306

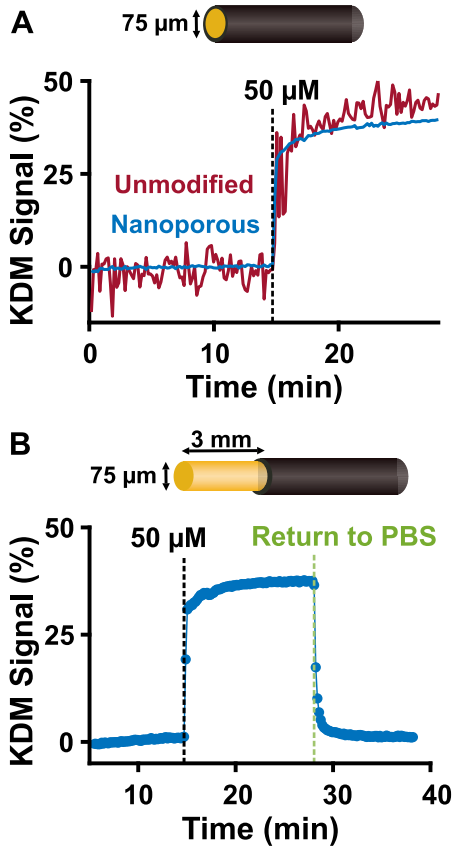

Figure 4. (A) Cutting insulated wires to expose a single circular surface, we produced 75 μm diameter "micro-disk" electrodes fabricated from unmodified gold and nanoporous gold. Both micro-disk electrodes respond immediately to the addition of 50 μM vancomycin in PBS. The sensor fabricated using nanoporous gold, however, yields a significantly improved signal to noise ratio. (B) The complex surface of the nanoporous gold does not significantly slow the equilibration of EAB sensors fabricated using this material. Shown here, for example, is the rapid response of a 3 mm long, 75 μm diameter nanoporous gold sensor when challenged in PBS with 50 μM vancomycin, followed by a return to baseline upon placing the sensor in target-free PBS.

(5 mV for in vitro data, 30 mV for in vivo data), this script calculates square wave voltammogram peak heights and KDM values. Raw data from this program is exported to Matlab for data analysis and presentation. To calculate cyclic voltammogram reduction peak areas, we use the on-board area calculation tool provided with the CH software interface.

RESULTS AND DISCUSSION

Because it can increase the microscopic surface area of gold wires up to 100-fold, we have applied an electrochemical alloying procedure, which creates a nanoporous gold layer on the surface.[34] In this technique, we apply cyclic voltammetry to alternatively deposit and strip away zinc metal (Figure S1). The cathodic potential sweep deposits zinc onto the gold surface, forming a layer of zinc and gold−zinc alloy.[35] The anodic sweep then removes the zinc from the surface, leaving behind a pitted gold surface.[35,36] Repeating this process produces a gold layer riven with nano- to microscale pores (Figure 1C), the smallest of which range from 30 to 500 nm in diameter (Figure 1D). The nanoporous gold fabrication technique produces a significantly greater microscopic surface area than either unmodified wire substrates or wires modified using the electrochemical roughening procedure[14] we have employed previously to produce dendrite morphologies (Figure 2A). Specifically, the alloying/dealloying technique that produces nanoporous gold achieves surface area enhancements of 75- to 100-fold relative to those seen for unmodified electrodes and 15- to 20-fold relative to dendrite electrodes (Figure 2B). The degree of surface area enhancement within a given alloying/dealloying batch is quite reproducible, as indicated by the near perfect overlap of cyclic voltammograms collected in sulfuric acid (Figure 2A).

The nanoporous gold electrodes' higher surface area increases the EAB sensor signal. As our test-bed demonstration of this, we prepared sensors that detect the antibiotic, vancomycin, which we fabricated using a range of aptamer deposition concentrations and times (Figure 3B). The sensors we fabricated using nanoporous electrodes produced consistently greater signaling current under all of the deposition conditions we investigated. Because the observed signal improvement for nanoporous wires plateaus at a 1 h incubation in the 1 μM aptamer (Figure 3B), we selected these parameters as our fabrication conditions moving forward. Compared to unmodified substrates, EAB sensors constructed on nanoporous electrodes exhibit higher signaling current from the aptamers' methylene blue redox reporter. For example, comparing cyclic voltammograms collected in phosphate-buffered saline, we see an approximately 25-fold increase in the methylene blue reduction peak for sensors fabricated using nanoporous electrodes (Figure 3C). We see similar signal enhancements when we compare square wave voltammetry peak currents (30-fold at 10 Hz), which, due to its sensitivity and reduction of charging current contributions, is the most ubiquitous approach for interrogating EAB sensors (Figure 3D).

The increase in the EAB signal we observe is smaller than the 75- to 100-fold increase in the microscopic surface area seen for nanoporous electrodes (Figure 2). This discrepancy, which is consistent with recent observations by Vesilinovic et al., who examined the impact of nanoporous gold surfaces on the signaling of a different class of electrochemical biosensors,[24] may result from two sources. First, hindered diffusion of the aptamer into the smallest pores in the matrix might reduce the number of aptamers per unit of the microscopic surface area. Consistent with this, the aptamer packing density on nanoporous gold is lower than that seen on unmodified gold. Fortunately, however, while lower aptamer packing density often is associated with increased EAB sensor degradation,[37] sensors fabricated on both nanoporous and unmodified substrates drift at similar rates (Figure S3). Second, charging currents can reduce square wave voltammogram peak height due to the greater capacitance associated with higher surface areas. Because charging currents increase with interrogation frequency,[38] baselines can impact peak signals at higher frequencies (Figure S4). Thus, effectively using high surface area substrates with EAB sensors (and other electrochemical sensors) requires a careful selection of interrogation frequency. Fortunately, however, the impact of capacitance on peak baselines is reduced when using smaller electrodes.

The enhanced signaling current provided by nanoporous electrodes enables significant EAB sensor miniaturization. To illustrate this, we first reduced the macroscopic surface area of a sensor by approximately 160-fold by fabricating it on an electrode produced by cutting an insulated gold wire to expose

https://doi.org/10.1021/acssensors.1c00354
ACS Sens. 2021, 6, 2299−2306

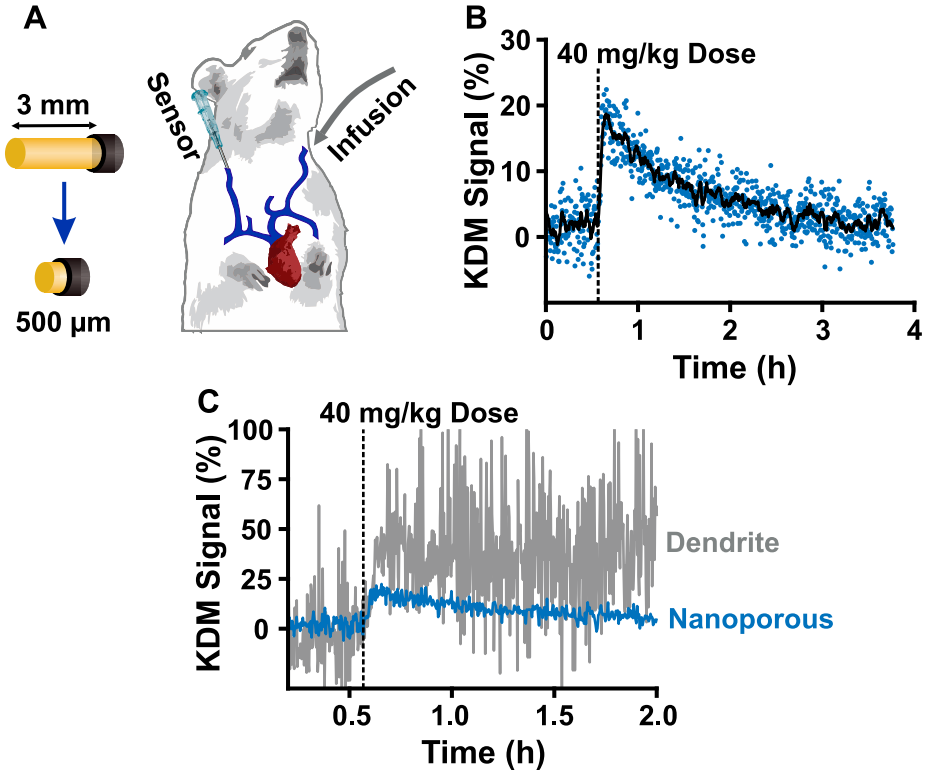

Figure 5. Use of nanoporous electrodes supports the miniaturization of in vivo EAB sensors. (A) Using a catheter, we place a miniaturized EAB sensor in the right jugular vein of an anesthetized rat and infuse vancomycin via the left jugular vein. (B) Shown here are in-vein measurements collected using a 75 μm diameter, 500 μm long vancomycin sensor fabricated on a nanoporous electrode. After collecting a 15 min baseline, we perform a 40 mg kg^{-1} IV injection of the drug. The resulting raw KDM signal (blue) and a 10-point rolling average (black) are shown. As expected, the sensor responds immediately to the vancomycin addition and then returns to baseline (zero) levels as the drug is cleared from the bloodstream over the course of a few hours. Using a calibration curve collected in undiluted bovine blood (Figure S6), we estimate the peak concentration in the jugular vein to be 8 μM (Figure S7). (C) We compare the raw KDM signal shown in the first panel to the signal collected using a dendrite-modified vancomycin sensor of the same macroscopic dimensions. In contrast to the nanoporous substrate (blue), the signal to noise of the dendrite-modified sensor (gray) is too poor to support measurements of drug delivery and clearance.

a 75 μm diameter disk. The resulting "microdisk" sensor produces easily measurable signal and target response in both its unmodified and nanoporous configurations (Figure 4A). The microdisk sensor fabricated using nanoporous gold, however, exhibited significantly reduced noise. For example, the 0.4% baseline noise (defined here as the relative standard deviation of the fluctuating signal seen in the absence of the target) seen for the nanoporous gold is more than nine times lower than that seen for the equivalent unmodified gold electrode. This improvement is so great that noise seen in vitro for a 75 μm nanoporous disk electrode is comparable to that seen for a 75 μm diameter, 3 mm long sensor fabricated on unmodified gold interrogated under the same conditions (Figure 4B).

Previous studies of nanoporous substrates have found that their complex morphology can slow the diffusion of materials to the electrode surface, in turn slowing sensor response or reducing its magnitude.[39−41] Fortunately, however, we have not found that this causes a significant limitation for detecting small-molecule targets, such as vancomycin. For example, when we exposed a sensor fabricated on nanoporous gold to 50 μM vancomycin in PBS, the sensor reached 90% of its final signaling current within 1 min (Figure 4B). Returning the sensor to target-free PBS, the signal returned to within 10% of the baseline in ∼2.5 min. In contrast, EAB sensor equilibration time does increase for higher-molecular-weight targets. Specifically, when challenging an EAB sensor[5] that responds to the 25 kDa protein, NGal, we observe 90% of signal saturation within ∼1 and ∼5 min for sensors fabricated on unmodified and nanoporous gold, respectively (Figure S5).

The improved signaling seen for sensors employing nanoporous gold electrodes supports experimentally significant reductions in the size of indwelling EAB sensors. For example, despite being six times smaller than our previously reported in vivo sensors, a 500 μm long, 75 μm diameter vancomycin-detecting EAB sensor fabricated on nanoporous gold still produces good baseline signal to noise (baseline standard deviation = 2%) when placed into the jugular of a live rat (Figure 5A).[1,2,12] In contrast, the signal associated with a sensor of the same size fabricated on a dendritic electrode was too poor to clearly resolve drug delivery and clearance (Figure 5B).

CONCLUSIONS

The electrochemical alloying/dealloying procedure applied here significantly improves the surface area, enabling reductions in the sensor size while maintaining effective performance. For example, the surface area enhancement's resulting increase in signal allowed us to reduce the length of the working electrode of an indwelling EAB sensor to just 500 μm, representing a 6-fold miniaturization of the working electrode relative to previous in vivo sensors in this class.[1,2,5,11,12,14] The resulting miniaturization offers a route

https://doi.org/10.1021/acssensors.1c00354
ACS Sens. 2021, 6, 2299−2306

forward for sensing systems where smaller working electrodes are critical, such as performing targeted measurements in brain regions and developing wearable, minimally invasive devices. The procedure is also simple, as it does not require clean room facilities and is compatible with any submersible gold surface. And unlike techniques such as co-sputtering and leaching of the alloyed foil, the approach is readily compatible with the wire electrode format we employ for in vivo sensors. It may likewise prove useful for other sensing architectures, such as electrodes embedded in fluidic channels, rod electrodes, and gold-functionalized micropipettes. Given this, we believe it could prove useful for enhancing the performance of a wide range of electrochemical sensors.

■ ASSOCIATED CONTENT

Supporting Information

The Supporting Information is available free of charge at https://pubs.acs.org/doi/10.1021/acssensors.1c00354.

Sensor drift; titrations; capacitance; and detection of nGal protein (PDF)

■ AUTHOR INFORMATION

Corresponding Author

Kevin W. Plaxco − *Department of Mechanical Engineering, University of California Santa Barbara, Santa Barbara, California 93106, United States; Center for Bioengineering and Department of Chemistry and Biochemistry, University of California Santa Barbara, Santa Barbara, California 93106, United States;* orcid.org/0000-0003-4772-8771; Email: kwp@ucsb.edu

Authors

Alex M. Downs − *Department of Mechanical Engineering, University of California Santa Barbara, Santa Barbara, California 93106, United States; Center for Bioengineering, University of California Santa Barbara, Santa Barbara, California 93106, United States*

Julian Gerson − *Department of Psychological and Brain Sciences, University of California Santa Barbara, Santa Barbara, California 93106, United States*

M. Nur Hossain − *Department of Physical and Environmental Sciences, University of Toronto Scarborough, Toronto, Ontario M1C1A4, Canada*

Kyle Ploense − *Department of Psychological and Brain Sciences, University of California Santa Barbara, Santa Barbara, California 93106, United States*

Michael Pham − *Department of Chemistry and Biochemistry, University of California Santa Barbara, Santa Barbara, California 93106, United States*

Heinz-Bernhard Kraatz − *Department of Physical and Environmental Sciences, University of Toronto Scarborough, Toronto, Ontario M1C1A4, Canada; Department of Chemistry, University of Toronto, Toronto, Ontario M5S 3H6, Canada;* orcid.org/0000-0002-7149-0110

Tod Kippin − *Department of Psychological and Brain Sciences and The Neuroscience Research Institute and Department of Molecular Cellular and Developmental Biology, University of California Santa Barbara, Santa Barbara, California 93106, United States*

Complete contact information is available at: https://pubs.acs.org/10.1021/acssensors.1c00354

Notes

The authors declare the following competing financial interest(s): K.W.P. discloses service on the scientific advisory boards of Diagnostic Biochips Inc. and Nutromics, both of which are developing applications related to this work.

■ ACKNOWLEDGMENTS

This work was funded by NIH grant R01AI145206 (to K.W.P.). This material is based upon work supported by the National Science Foundation Graduate Research Fellowship under Grant No. 1650114 (A.M.D.). The content of the information does not necessarily reflect the position or the policy of the Government and no official endorsement should be inferred. The authors also acknowledge financial contributions from the Natural Sciences and Engineering Research Council of Canada (NSERC-RGPIN-2016-06122 to H.-B.K.) and the University of Toronto at Scarborough. A portion of this work was performed in the UCSB Nanofabrication Facility, an open access laboratory.

■ REFERENCES

(1) Arroyo-Currás, N.; Somerson, J.; Vieira, P. A.; Ploense, K. L.; Kippin, T. E.; Plaxco, K. W. Real-time measurement of small molecules directly in awake, ambulatory animals. *Proc. Natl. Acad. Sci. U.S.A.* **2017**, *114*, 645−650.

(2) Dauphin-Ducharme, P.; Yang, K.; Arroyo-Currás, N.; Ploense, K. L.; Zhang, Y.; Gerson, J.; Kurnik, M.; Kippin, T. E.; Stojanovic, M. N.; Plaxco, K. W. Electrochemical aptamer-based sensors for improved therapeutic drug monitoring and high-precision, feedback-controlled drug delivery. *ACS Sens.* **2019**, *4*, 2832−2837.

(3) Idili, A.; Arroyo-Currás, N.; Ploense, K. L.; Csordas, A. T.; Kuwahara, M.; Kippin, T. E.; Plaxco, K. W. Seconds-resolved pharmacokinetic measurements of the chemotherapeutic irinotecan in situ in the living body. *Chem. Sci.* **2019**, *10*, 8164−8170.

(4) Swensen, J. S.; Xiao, Y.; Ferguson, B. S.; Lubin, A. A.; Lai, R. Y.; Heeger, A. J.; Plaxco, K. W.; Soh, H. T. Continuous, real-time monitoring of cocaine in undiluted blood serum via a microfluidic, electrochemical aptamer-based sensor. *J. Am. Chem. Soc.* **2009**, *131*, 4262−4266.

(5) Parolo, C.; Idili, A.; Ortega, G.; Csordas, A.; Hsu, A.; Arroyo-Currás, N.; Yang, Q.; Ferguson, B. S.; Wang, J.; Plaxco, K. W. Real-time monitoring of a protein biomarker. *ACS Sens.* **2020**, *5*, 1877−1881.

(6) Liu, Y.; Kwa, T.; Revzin, A. Simultaneous detection of cell-secreted tnf-α and ifn-γ using micropatterned aptamer-modified electrodes. *Biomaterials* **2012**, *33*, 7347−7355.

(7) Mayer, M. D.; Lai, R. Y. Effects of redox label location on the performance of an electrochemical aptamer-based tumor necrosis factor-alpha sensor. *Talanta* **2018**, *189*, 585−591.

(8) Idili, A.; Gerson, J.; Parolo, C.; Kippin, T.; Plaxco, K. W. An electrochemical aptamer-based sensor for the rapid and convenient measurement of l-tryptophan. *Anal. Bioanal. Chem.* **2019**, *411*, 4629−4635.

(9) Idili, A.; Parolo, C.; Ortega, G.; Plaxco, K. W. Calibration-free measurement of phenylalanine levels in the blood using an electrochemical aptamer-based sensor suitable for point-of-care applications. *ACS Sens.* **2019**, *4*, 3227−3233.

(10) White, R. J.; Phares, N.; Lubin, A. A.; Xiao, Y.; Plaxco, K. W. Optimization of electrochemical aptamer-based sensors via optimization of probe packing density and surface chemistry. *Langmuir* **2008**, *24*, 10513−10518.

(11) Arroyo-Currás, N.; Dauphin-Ducharme, P.; Ortega, G.; Ploense, K. L.; Kippin, T. E.; Plaxco, K. W. Subsecond-resolved molecular measurements in the living body using chronoamperometrically interrogated aptamer-based sensors. *ACS Sens.* **2018**, *3*, 360−366.

(12) Arroyo-Currás, N.; Ortega, G.; Copp, D. A.; Ploense, K. L.; Plaxco, Z. A.; Kippin, T. E.; Hespanha, J. P.; Plaxco, K. W. High-precision control of plasma drug levels using feedback-controlled dosing. *ACS Pharmacol. Transl. Sci.* **2018**, *1*, 110−118.
(13) Li, H.; Li, S.; Dai, J.; Li, C.; Zhu, M.; Li, H.; Lou, X.; Xia, F.; Plaxco, K. W. High frequency, calibration-free molecular measurements in situ in the living body. *Chem. Sci.* **2019**, *10*, 10843−10848.
(14) Arroyo-Currás, N.; Scida, K.; Ploense, K. L.; Kippin, T. E.; Plaxco, K. W. High surface area electrodes generated via electrochemical roughening improve the signaling of electrochemical aptamer-based biosensors. *Anal. Chem.* **2017**, *89*, 12185−12191.
(15) Kashefi-Kheyrabadi, L.; Mehrgardi, M. A. Aptamer-based electrochemical biosensor for detection of adenosine triphosphate using a nanoporous gold platform. *Bioelectrochemistry* **2013**, *94*, 47−52.
(16) Qiu, H.; Sun, Y.; Huang, X.; Qu, Y. A sensitive nanoporous gold-based electrochemical aptasensor for thrombin detection. *Colloids Surf., B* **2010**, *79*, 304−308.
(17) Liu, J.; Wagan, S.; Dávila Morris, M.; Taylor, J.; White, R. J. Achieving reproducible performance of electrochemical, folding aptamer-based sensors on microelectrodes: Challenges and prospects. *Anal. Chem.* **2014**, *86*, 11417−11424.
(18) Yang, W.; Gerasimov, J. Y.; Lai, R. Y. Folding-based electrochemical DNA sensor fabricated on a gold-plated screen-printed carbon electrode. *Chem. Commun.* **2009**, *20*, 2902−2904.
(19) Kiani, A.; Fard, E. N. Fabrication of palladium coated nanoporous gold film electrode via underpotential deposition and spontaneous metal replacement: A low palladium loading electrode with electrocatalytic activity. *Electrochim. Acta* **2009**, *54*, 7254−7259.
(20) Ji, C.; Searson, P. C. Fabrication of nanoporous gold nanowires. *Appl. Phys. Lett.* **2002**, *81*, 4437−4439.
(21) Rouya, E.; Reed, M. L.; Kelly, R. G.; Bart-Smith, H.; Begley, M.; Zangari, G. Synthesis of nanoporous gold structures via dealloying of electroplated au-ni alloy films. *ECS Trans.* **2007**, *6*, 41−50.
(22) Cherevko, S.; Chung, C.-H. Direct electrodeposition of nanoporous gold with controlled multimodal pore size distribution. *Electrochem. Commun.* **2011**, *13*, 16−19.
(23) Seker, E.; Reed, M. L.; Begley, M. R. Nanoporous gold: Fabrication, characterization, and applications. *Materials* **2009**, *2*, 2188−2215.
(24) Veselinovic, J.; AlMashtoub, S.; Nagella, S.; Seker, E. Interplay of effective surface area, mass transport, and electrochemical features in nanoporous nucleic acid sensors. *Anal. Chem.* **2020**, *92*, 10751−10758.
(25) Matharu, Z.; Daggumati, P.; Wang, L.; Dorofeeva, T. S.; Li, Z.; Seker, E. Nanoporous-gold-based electrode morphology libraries for investigating structure−property relationships in nucleic acid based electrochemical biosensors. *ACS Appl. Mater. Interfaces* **2017**, *9*, 12959−12966.
(26) Zhu, Y.; Zhou, C.; Yan, X.; Yan, Y.; Wang, Q. Aptamer-functionalized nanoporous gold film for high-performance direct electrochemical detection of bisphenol a in human serum. *Anal. Chim. Acta* **2015**, *883*, 81−89.
(27) Xia, Y.; Huang, W.; Zheng, J.; Niu, Z.; Li, Z. Nonenzymatic amperometric response of glucose on a nanoporous gold film electrode fabricated by a rapid and simple electrochemical method. *Biosens. Bioelectron.* **2011**, *26*, 3555−3561.
(28) Downs, A. M.; Gerson, J.; Ploense, K. L.; Plaxco, K. W.; Dauphin-Ducharme, P. Subsecond-resolved molecular measurements using electrochemical phase interrogation of aptamer-based sensors. *Anal. Chem.* **2020**, *92*, 14063−14068.
(29) Ferguson, B. S.; Hoggarth, D. A.; Maliniak, D.; Ploense, K.; White, R. J.; Woodward, N.; Hsieh, K.; Bonham, A. J.; Eisenstein, M.; Kippin, T. E.; Plaxco, K. W.; Soh, H. T. Real-time, aptamer-based tracking of circulating therapeutic agents in living animals. *Sci. Transl. Med.* **2013**, *5*, No. 213ra165.
(30) Institute of Laboratory Animal Resources (US). Committee on Care, & Use of Laboratory Animals. *Guide for the Care and Use of Laboratory Animals*; National Academies Press: Washington (DC), 2011.
(31) Curtis, S. D.; Ploense, K. L.; Kurnik, M.; Ortega, G.; Parolo, C.; Kippin, T. E.; Plaxco, K. W.; Arroyo-Currás, N. Open source software for the real-time control, processing, and visualization of high-volume electrochemical data. *Anal. Chem.* **2019**, *91*, 12321−12328.
(32) Xiao, X.; Si, P.; Magner, E. An overview of dealloyed nanoporous gold in bioelectrochemistry. *Bioelectrochemistry* **2016**, *109*, 117−126.
(33) Trasatti, S.; A P, O. Real surface area measurements in electrochemistry. *J. Electroanal. Chem.* **1992**, *327*, 353−376.
(34) Hossain, M. N.; Liu, Z.; Wen, J.; Chen, A. Enhanced catalytic activity of nanoporous au for the efficient electrochemical reduction of carbon dioxide. *Appl. Catal., B* **2018**, *236*, 483−489.
(35) Jia, F.; Yu, C.; Ai, Z.; Zhang, L. Fabrication of nanoporous gold film electrodes with ultrahigh surface area and electrochemical activity. *Chem. Mater.* **2007**, *19*, 3648−3653.
(36) van der Zalm, J.; Chen, S.; Huang, W.; Chen, A. Review—recent advances in the development of nanoporous au for sensing applications. *J. Electrochem. Soc.* **2020**, *167*, No. 037532.
(37) Deng, M.; Li, M.; Li, F.; Mao, X.; Li, Q.; Shen, J.; Fan, C.; Zuo, X. Programming accessibility of DNA monolayers for degradation-free whole-blood biosensors. *ACS Mater. Lett.* **2019**, *1*, 671−676.
(38) Ramaley, L.; Krause, M. S. Theory of square wave voltammetry. *Anal. Chem.* **1969**, *41*, 1362−1365.
(39) Macias, G.; Ferré-Borrull, J.; Pallarès, J.; Marsal, L. F. Effect of pore diameter in nanoporous anodic alumina optical biosensors. *Analyst* **2015**, *140*, 4848−4854.
(40) Arshavsky Graham, S.; Boyko, E.; Salama, R.; Segal, E. Mass transfer limitations of porous silicon-based biosensors for protein detection. *ACS Sens.* **2020**, *5*, 3058−3069.
(41) Collinson, M. M. Nanoporous gold electrodes and their applications in analytical chemistry. *ISRN Anal. Chem.* **2013**, *2013*, No. 692484.

https://doi.org/10.1021/acssensors.1c00354
ACS Sens. 2021, 6, 2299−2306